
ANALYSIS AND SIMULATION OF A COUPLED DIFFUSION BASED IMAGE DENOISING MODEL

A PREPRINT

Subit K. Jain
School of Basic Sciences
Indian Institute of Technology Mandi
PIN 175005, INDIA
jain.subit@gmail.com

Sudeb Majee
School of Basic Sciences
Indian Institute of Technology Mandi
PIN 175005, INDIA
sudebmajee@gmail.com

Rajendra K. Ray
School of Basic Sciences
Indian Institute of Technology Mandi
PIN 175005, INDIA
rajendra@iitmandi.ac.in

Ananta K. Majee
Department of Mathematics
Indian Institute of Technology Delhi
PIN 110016, INDIA
majee@maths.iitd.ac.in

August 8, 2019

ABSTRACT

In this study, a new coupled Partial Differential Equation (CPDE) based image denoising model incorporating space-time regularization into non-linear diffusion is proposed. This proposed model is fitted with additive Gaussian noise which performs efficient image smoothing along with the preservation of edges and fine structures. For this purpose, we propose a new functional minimization framework to remove the image noise, which results in solving a system of three partial differential equations (PDEs). Our proposed model is dissimilar from the existing CPDE models as it includes two additional evolution equations to handle edge strength function and data fidelity term. These two evolution equations control the smoothing process and force the resultant denoised solution to be close to the initial solution. To the best of our knowledge, the proposed model is the only work, which deciphers the combined effect of both the terms using separate PDEs. Furthermore, we establish the existence and uniqueness of a weak solution of the proposed system using the time discretization method with H^1 initial data. Finally, we used a generalized weighted average finite difference scheme to efficiently solve the coupled system and experiment results show the effectiveness of the proposed CPDE model.

Keywords Image denoising · Space-Time regularization · Non-linear diffusion · Semi discretization · Weak solution

1 Introduction

Reduction of generated noise in the restored images without loss of spatial resolution is highly desirable in many image processing applications. The behavior of noise reduction methods is entirely different for large areas with well-defined borders as well as for poorly defined borders. It has been observed that the goal of noise reduction with feature preservation and applicability to the multiple acquisition systems is difficult to achieve through a single method [1, 2]. Therefore, the accurate reconstruction of key features in an image from the noisy measurement is the main objective of our study.

The noise caused by image acquisition devices is often modeled by Gaussian random distribution. Generally, the degraded image can be modeled as

$$J = I + \eta, \tag{1}$$

where J is the noisy image, degraded by Gaussian noise with zero mean, defined on an image space Ω , and I depicts the clean image, and η is the additive noise function. Our main task is to obtain the reconstructed image from the observed noisy image.

In recent years, PDE based methods have become widely applicable for noise removal and signal reconstruction, due to their well-established mathematical properties and their general wellposedness [1, 3, 4, 5, 6, 7, 8]. Obtaining the steady-state solution is the basic objective of PDE based image restoration problem. This goal can be achieved through two approaches. In the first approach, we directly find a steady state solution of the diffusion model. Whereas in the second approach, the steady-state solution is obtained from the evolution equation of the Euler-Lagrange equation associated with the energy functional. Several techniques are employed to handle the challenges posed by restoration problems. The availability of vast literature does not allow us to review all of them. However, we briefly report some of the robust techniques such that anisotropic diffusion [3, 6, 7, 9, 10, 11], fourth order diffusion [12, 13, 14], complex diffusion [15, 16] and variational based methods [17, 18, 19, 20, 21, 22]. In all of the above-mentioned methods, spatial regularization is used for diffusion function, which is not able to inject the past information into the iterative process of diffusion. Therefore, the scheme may not be effective for solving image denoising problems which contain huge textures in their image domain. To handle this, applications of time-delay regularization with spatial regularization are also available in the literature [23, 24, 25, 26, 27, 28]. The space-time regularization is more suitable approach than Gaussian filtering as it enables to incorporate the information obtained along with the scales into the diffusion process. This type of regularization is used to recover fine structures, especially for images degraded with higher noise levels. Hence apart from a single PDE based approaches, several studies are utilizing coupled PDE to perform image restoration [29]. In this regard, Nitzberg and Shiota [27] introduce a delay in time to calculate diffusivity term as,

$$I_t = \nabla \left(\frac{1}{1+u^2} \nabla I \right), \quad \text{in } \Omega \times (0, T), \quad (2)$$

where u in diffusion function is calculated using the relation: $u_t = \varphi(G_\xi * |\nabla I|^2 - u)$ and T is a fixed time. Here, ξ is a positive smoothing parameter required for the analytical well-posedness of the model. So, the term u updates the edge information from the gradient of the updated image and past information of itself. Hence, instead of spatial regularization, u represents a temporal regularization in the formation of the diffusion term. This coupled PDE system is quite similar to the Perona-Malik model [10] as there is no spatial smoothing term. In [27], the authors show that the coupled PDE system admits a unique classical solution (I, u) in any dimension and satisfy the maximum principle. They also explain that the system does not produce spurious features. A similar idea of coupled PDE system using time-delay regularization is proposed by Luo et al. [26], for image denoising. They propose the estimation of a better edge map by substituting the isotropic diffusion by a nonlinear diffusion equation, to produce a regularized version of the diffusion function for image smoothing. Subsequently, Guo et al. [25] propose and analyze the well-posedness of a reaction-diffusion system for image denoising. They deploy the H^{-1} norm instead of $L1/L2$ norm with the total variation model [30], to preserve the oscillatory and texture patterns, as follows,

$$E_{H^{-1}} = \int_{\Omega} |\nabla I| d\Omega + \lambda \|J - I\|_{H^{-1}(\Omega)}^2. \quad (3)$$

Here, $\|\cdot\|_{H^{-1}(\Omega)}^2 = \int_{\Omega} |\nabla \Delta^{-1}(\cdot)|^2 d\Omega$. This model is efficient for denoising and decomposing the image into cartoon plus texture. Now evolution equation of the Euler-Lagrange equation of the above functional, in which two PDEs are interacting with each other to calculate noise fidelity term, can be given as,

$$\left. \begin{aligned} I_t &= \nabla \left(\frac{\nabla I}{|\nabla I|} \right) - 2\lambda v, & \text{in } \Omega \times (0, T), \\ v_t &= \Delta v - (J - I), & \text{in } \Omega \times (0, T). \end{aligned} \right\} \quad (4)$$

In the above model, another PDE is used to calculate the fidelity (v) term efficiently. The main difficulty with this model is that the term $\frac{1}{|\nabla I|}$ is singular when $|\nabla I| = 0$. However, the numerical simulations involve the regularization of $|\nabla I|$ with $|\nabla I| + \varepsilon$. A good survey on the existing CPDE approaches can be found in [29].

The objective of the present work is to systematically develop a new framework of coupled nonlinear diffusion model. The present approach differs from previous existing CPDE based works as it utilizes separate evolution equations to calculate edge strength function as well as the data fidelity term. The originality of the proposed coupled non-linear PDEs algorithm lies in the combined effect of:

- i. diffusion coefficient with space-time regularization instead of space regularization only;
- ii. H^{-1} norm based time-varying fidelity term.

Moreover, due to the interest in theoretical research, we establish the well-posedness of the proposed CPDE model (10)-(13). To prove the well-posedness, we use a time discretization method along with essential a-priori estimates and classical results of compact inclusion in Sobolev spaces [31]; by utilizing some important inequalities, lemmas and theorems [32] and then tends the time discretization parameter to zero. This imparts a major role of this study as it is very important for the numerical computation. Further, to simulate the image denoising, we apply a higher order accurate generalized weighted average finite difference scheme with an advanced iterative solver (Hybrid Bi-Conjugate Gradient Stabilized method) to solve the algebraic system of equations generated from the discretization process [33]. The image quality of denoised images using the proposed CPDE model is compared against several existing non-linear diffusion models, variational based models and CPDE based models. In practice, our calculations indicate that the proposed approach allows effective image smoothing on fine scales even when the images are degraded with a higher level of noise.

The rest of the paper is arranged in the following sequence. Section 2 describes the mathematical formulation of the proposed coupled nonlinear diffusion model. In section 3 we establish the existence and uniqueness of a weak solution to the proposed PDE model. Section 4 shows an appropriate numerical realization in terms of higher order accurate implicit finite difference scheme. Numerical validation of the proposed approach using experimental study is carried out in section 5. At the end, we summarize our observations in section 6.

2 Proposed Coupled Diffusion Model

The main aim of this work is to present a novel approach for image smoothing by the evolution of coupled non-linear PDEs. Among the existing CPDE based models mentioned in the previous section, the choices of diffusion function and fidelity term include the space and time regularization. Numerical simulations and experimental results depict that the space-time regularization plays a important role in the quality of recovered images degraded by noise. We note that all of these existing coupled PDEs described in the last section utilizes the time-delay regularization to calculate either diffusion coefficient or fidelity term, and sometimes fail to preserve significant contents of the image. Thus, one issue of these smoothing algorithms is how to design a non-linear diffusion algorithm, which can remove the noise and preserve the small features, simultaneously. For this purpose, inspired by the impressive performance of time-delay regularization in image smoothing, we proposed the following energy functional:

$$\min E_u(I) = \int_{\Omega} \frac{1}{2} g(u) |\nabla I|^2 d\Omega + \lambda \|I_0 - I\|_{H^{-1}(\Omega)}^2, \quad (5)$$

where I_0 represents the high pass filtered version of image J and λ is weight parameter. Generally, λ is chosen to be inversely proportional to the variance of the noise in the given image. The first term represents a regularizing term producing a smooth varying variable function. The term $g(u)$ serves the purpose of detecting the edges in the image, and u is the edge variable. The second term forces the denoised solution I to be a close approximation to I_0 and referred to as data fidelity term. In the data fidelity term, we have replaced L^2 norm of $(I_0 - I)$ by H^{-1} norm to preserve the oscillatory and texture information more appropriately in a denoised image. The solution of the above minimization problem (5) can be given by the steady-state of the Euler-Lagrange equation for $E_u(I)$:

$$\frac{1}{2\lambda} \nabla(g(u) \nabla I) = \Delta^{-1}(I_0 - I). \quad (6)$$

This is equivalent to following equations,

$$\left. \begin{aligned} \nabla(g(u) \nabla I) - 2\lambda v &= 0, \\ \nabla(\nabla v) - (I_0 - I) &= 0. \end{aligned} \right\} \quad (7)$$

To this end, we consider the function u as the following,

$$u_t = \alpha (|\nabla I_{\xi}|^2 - u + \frac{\beta^2}{2} \Delta u), \quad (8)$$

where $\alpha > 0$ and $\beta > 0$ are parameters to be specified; average time delay (α^{-1}) and amount of the spatial smoothing (β) control the deformation and smoothness of the edge information and chosen as described in [27]. And, $I_{\xi} = G_{\xi}(X) * I$ where two dimensional Gaussian function $G_{\xi}(\cdot)$ at each pixel, $X \in \Omega$ is adopted as,

$$G_{\xi}(X) = \left(\xi\sqrt{2\pi}\right)^{-1} \exp\left(\frac{-|X|^2}{2\xi^2}\right), \quad (9)$$

where “ $*$ ” denote the convolution operator and $\xi > 0$ is the standard deviation of the function. Finally, our proposed model in which a set of PDEs interacting with each other, can be expressed as follows,

$$\frac{\partial I}{\partial t} = \nabla(g(u)\nabla I) - 2\lambda v, \quad \text{in } \Omega_T := (0, T) \times \Omega, \quad (10)$$

$$\frac{\partial u}{\partial t} = \alpha(h(|\nabla I_\xi|^2) - u + \frac{\beta^2}{2} \Delta u), \quad \text{in } \Omega_T, \quad (11)$$

$$\frac{\partial v}{\partial t} = \nabla(\nabla v) - (I_0 - I), \quad \text{in } \Omega_T, \quad (12)$$

$$I(0, x) = I_0(x), \quad v(0, x) = 0, \quad u(0, x) = G_\xi * |\nabla I_0|^2, \quad \text{in } \Omega. \quad (13)$$

In the above model, diffusion coefficient $g(u)$ is chosen as

$$g(u) = \frac{1}{1 + \frac{|G_\xi * u|}{k^2}}, \quad (14)$$

where $k > 0$ is a threshold parameter, and u represents edge strength at each iteration. Note that we replace $|\nabla I_\xi|^2$ in (8) by $h(|\nabla I_\xi|^2)$, where h being a sort of truncation, see [24]. Our proposed model is different from the models reported earlier in [29], as it yields two separate evolution equations (PDEs) to handle the diffusion coefficient and data fidelity term. These two evolution equations are responsible for stopping the image smoothing at the edges as well as textures and forces the resulting solution to be a close approximation to the given initial image. The proposed model is in a spirit similar to the reaction-diffusion model equation in [25]; however, the diffusion function is very different in our case. In (10)-(13), the smoothing equation (10) has different edge variable u and fidelity term v , obtained from two different PDEs. The data fidelity term between I and I_0 can be handled by function v , which can be obtained from equation (12). Whereas the function u in the diffusion coefficient can be calculated from equation (11). In summary, the proposed model achieves a suitable edge map and fidelity between noisy image and restored image at each iteration, which ultimately leads to quality denoising results. Hence, the proposed model provides a potential approach for image noise removal and enhancement.

3 Existence and uniqueness of weak solution

In this section, we establish the well-posedness of (10)-(13) with Dirichlet’s boundary condition for the fidelity variable and Neumann’s boundary condition for other two variables. Furthermore, for simplicity we choose all the constants involved in the equations (10)-(13) equals to 1. Note that, $h : \mathbb{R}^+ \rightarrow \mathbb{R}^+$ is a bounded, Lipschitz continuous function with Lipschitz constant c_h such that

$$\delta \leq h(\tilde{u}) \leq 1 \quad \forall \tilde{u} \in \mathbb{R}^+, \quad (15)$$

for some $\delta > 0$. Also from (14) we observe that, $g : \mathbb{R} \rightarrow \mathbb{R}^+$ is a bounded, decreasing and Lipschitz continuous function with Lipschitz constant $\frac{C_\xi}{k^2}$. Moreover, $g(0) = 1$ and $\lim_{u \rightarrow +\infty} g(u) = 0$.

3.1 Technical framework

We denote by $H^k(\Omega)$, k is a positive integer, the set of all functions $I : \Omega \rightarrow \mathbb{R}$ such that I and its distributional derivatives $\frac{\partial^m I}{\partial x^m}$ of order $|m| = \sum_{j=1}^2 m_j \leq k$ all belongs to $L^2(\Omega)$. $H^k(\Omega)$ is a Hilbert space endowed with the norm

$$\|I\|_{H^k} := \|I\|_{H^k(\Omega)} = \left(\sum_{|m| \leq k} \int_{\Omega} \left| \frac{\partial^m I}{\partial x^m} \right|^2 dx \right)^{1/2}.$$

We denote by $L^p(0, T; H^k(\Omega))$, $p > 1$ and k is a positive integer, the set of all measurable functions $I : [0, T] \rightarrow H^k(\Omega)$ such that

$$\|I\|_{L^p(0, T; H^k(\Omega))} := \left(\int_0^T \|I(t)\|_{H^k(\Omega)}^p dt \right)^{1/p} < \infty.$$

We denote by $H^1(\Omega)'$ the dual of $H^1(\Omega)$, and $H^{-1}(\Omega)$ the dual of $H_0^1(\Omega)$. For any $f \in H^1(\Omega)'$, we define a norm as

$$\|f\|_{H^1(\Omega)'} = \left\{ \sup \langle f, u \rangle : u \in H^1(\Omega), \|u\|_{H^1(\Omega)} \leq 1 \right\}.$$

We introduce the solution space $W(0, T) := W_1(0, T) \times W_1(0, T) \times W_2(0, T)$ for the problem (10)-(13), where

$$\begin{aligned} W_1(0, T) &= \left\{ w : w \in L^2(0, T; H^1(\Omega)), \frac{\partial w}{\partial t} \in L^2(0, T; (H^1(\Omega))') \right\}, \\ W_2(0, T) &= \left\{ w : w \in L^2(0, T; H_0^1(\Omega)), \frac{\partial w}{\partial t} \in L^2(0, T; H^{-1}(\Omega)) \right\}. \end{aligned}$$

Note that, the space $W_i(0, T)$ ($i = 1, 2$) is a Hilbert space for the graph norm, see [34].

Definition 3.1 (Weak solution) Let $I_0 \in H^1(\Omega)$. We say that a triple (I, u, v) is a weak solution of (10)-(13) if

(i) $I, u \in W_1(0, T)$, and $v \in W_2(0, T)$.

(ii) For all $\Psi \in H^1(\Omega)$ and $\Phi \in H_0^1(\Omega)$, there holds

$$\int_0^T \left\langle \frac{\partial I}{\partial t}, \Psi \right\rangle dt + \int_{\Omega_T} g(u) \nabla I \cdot \nabla \Psi \, dx \, dt + 2 \int_{\Omega_T} v \Psi \, dx \, dt = 0, \quad (16)$$

$$\begin{aligned} \int_0^T \left\langle \frac{\partial u}{\partial t}, \Psi \right\rangle dt - \int_{\Omega_T} h(|\nabla I_\xi|^2) \Psi \, dx \, dt + \int_{\Omega_T} u \Psi \, dx \, dt \\ + \int_{\Omega_T} \nabla u \cdot \nabla \Psi \, dx \, dt = 0, \end{aligned} \quad (17)$$

$$\int_0^T \left\langle \frac{\partial v}{\partial t}, \Phi \right\rangle dt + \int_{\Omega_T} \nabla v \cdot \nabla \Psi \, dx \, dt + \int_{\Omega_T} (I_0 - I) \Psi \, dx \, dt = 0. \quad (18)$$

(iii) (13) holds.

3.2 Discretized system and existence of its weak solution

To prove existence of a weak solution of (10)-(13), we use semi discretization in time with a semi-implicit Euler method. Let $0 = t_0 < t_1 < t_2 \cdots < t_N = T$ be a uniform partition of $[0, T]$ with time-step size $\tau = \frac{T}{N}$ for some $N \in \mathbb{N}^+$, i.e, $t_n = \tau n$ for $0 \leq n \leq N$. For simplicity, in the following we write L^2, H^1, H_0^1 instead of $L^2(\Omega), H^1(\Omega), H_0^1(\Omega)$ respectively. We may then consider time discretization of (10)-(13) as follows: for $0 \leq n \leq N-1$, $\forall \Psi \in H^1$, and $\forall \Phi \in H_0^1$ iterate:

(i) compute $u_{n+1} \in H^1$ such that

$$\begin{aligned} \left(\frac{1}{\tau} (u_{n+1} - u_n), \Psi \right)_{L^2} + (\nabla u_{n+1}, \nabla \Psi)_{L^2} + (u_{n+1}, \Psi)_{L^2} \\ = (h(|\nabla G_\xi * I_n|^2), \Psi)_{L^2}, \end{aligned} \quad (19)$$

(ii) compute $v_{n+1} \in H_0^1$ such that

$$\left(\frac{1}{\tau} v_{n+1}, \Phi \right)_{L^2} + (\nabla v_{n+1}, \nabla \Phi)_{L^2} = \left(\frac{1}{\tau} v_n - (I_0 - I_n), \Phi \right)_{L^2} \quad (20)$$

(iii) compute $I_{n+1} \in H^1$

$$\left(\frac{1}{\tau} I_{n+1}, \Psi \right)_{L^2} + (g(u_n) \nabla I_{n+1}, \nabla \Psi)_{L^2} = \left(\frac{1}{\tau} I_n - 2v_n, \Psi \right)_{L^2}. \quad (21)$$

Thanks to (15), the existence of u_{n+1} resp. v_{n+1} in step (i) resp. in step (ii) easily follows from Lax-Milgram lemma. Moreover, these solutions are unique. To show the well-posedness of (21), we use standard Lax-Milgram lemma. Define a continuous bilinear form $\mathcal{C} : H^1 \times H^1 \rightarrow \mathbb{R}$, and a linear bounded functional $\ell : H^1 \rightarrow \mathbb{R}$ as

$$\mathcal{C}(\Theta, \Psi) = \left(\frac{1}{\tau} \Theta, \Psi \right)_{L^2} + (g(u_n) \nabla \Theta, \nabla \Psi)_{L^2}; \quad \ell(\Psi) = \left(\frac{1}{\tau} I_n - 2v_n, \Psi \right)_{L^2}. \quad (22)$$

Then, by Lax-Milgram lemma, there exists a unique $I_{n+1} \in H^1$ satisfying (21) provided \mathcal{C} is H^1 -coercive. Indeed, thanks to Gagliardo-Nirenberg inequality, there exists a constant $C > 0$, depending only on Ω and G_ξ , such that

$$\frac{1}{1 + \frac{C \|u_n\|_{H^1}}{k^2}} \leq g(u_n), \quad (23)$$

and hence $\mathcal{C}(\Psi, \Psi) \geq \frac{1}{\tau} \|\Psi\|_{L^2}^2 + \frac{1}{1 + \frac{C \|u_n\|_{H^1}}{k^2}} \|\nabla \Psi\|_{L^2}^2 \geq \tilde{C} \|\Psi\|_{H^1}^2$ where $\tilde{C} := \min \left\{ \frac{1}{\tau}, \frac{1}{1 + \frac{C \|u_n\|_{H^1}}{k^2}} \right\}$ yielding the H^1 -coercivity of \mathcal{C} .

3.3 A-priori estimates

Let $0 \leq n \leq N-1$. Choose $\Psi = u_{n+1}$ as test function in (19) and use the algebraic identity

$$\langle a, a-b \rangle = \frac{1}{2}(|a|^2 - |b|^2 + |a-b|^2), \quad \forall a, b \in \mathbb{R}^p \ (p \geq 1), \quad (24)$$

Cauchy-Schwarz and Young's inequalities, (15), and then sum over $n = 0, 1, 2, \dots, j-1$ with $1 \leq j \leq N$. The result is

$$\begin{aligned} \|u_j\|_{L^2}^2 + \sum_{n=0}^{j-1} \|u_{n+1} - u_n\|_{L^2}^2 + 2\tau \sum_{n=0}^{j-1} \|\nabla u_{n+1}\|_{L^2}^2 \\ \leq \|u_0\|_{L^2}^2 + |\Omega| \sum_{n=0}^{j-1} \tau \leq \|u_0\|_{L^2}^2 + T|\Omega|. \end{aligned} \quad (25)$$

Hence, there exists a constant $C_1 > 0$, independent of $\tau > 0$, such that

$$\max_{1 \leq j \leq N} \|u_j\|_{L^2}^2 + \sum_{n=0}^{N-1} \|u_{n+1} - u_n\|_{L^2}^2 + 2\tau \sum_{n=0}^{N-1} \|\nabla u_{n+1}\|_{L^2}^2 \leq C_1. \quad (26)$$

Similarly, by choosing (formally) $\Psi = -\Delta u_{n+1}$ in (19) and using the integration by parts formula, (24), Cauchy-Schwarz and Young's inequalities, (15), and then summing over $n = 0, 1, 2, \dots, j-1$ with $1 \leq j \leq N$, we obtain

$$\max_{1 \leq j \leq N} \|\nabla u_j\|_{L^2}^2 + \sum_{n=0}^{N-1} \|\nabla(u_{n+1} - u_n)\|_{L^2}^2 + \tau \sum_{n=0}^{N-1} \|\Delta u_{n+1}\|_{L^2}^2 \leq C_2, \quad (27)$$

where $C_2 > 0$ is a constant, independent of $\tau > 0$. In view of (26) and (27), there exists a constant $C_3 > 0$, independent of τ , such that

$$\max_{0 \leq j \leq N} \|u_j\|_{H^1(\Omega)} \leq C_3. \quad (28)$$

Therefore, from (23), the positive lower bound for $g(u_n)$ is given by

$$\nu := \frac{1}{1 + \frac{CC_3}{k^2}} \leq g(u_n) \quad (0 \leq n \leq N). \quad (29)$$

Again, one can use the test function $\Phi = v_{n+1}$ and $\Phi = -\Delta v_{n+1}$ (formally) in (20), and proceed as above (under the cosmetic changes) to obtain ($1 \leq j \leq N$):

$$\begin{aligned} \|v_j\|_{L^2}^2 + \sum_{n=0}^{j-1} \|v_{n+1} - v_n\|_{L^2}^2 + \tau \sum_{n=0}^{j-1} \|\nabla v_{n+1}\|_{L^2}^2 \\ \leq \|v_0\|_{L^2}^2 + C_P^2 T \|I_0\|_{L^2}^2 + \tau C_P^2 \sum_{n=0}^{j-1} \|I_n\|_{L^2}^2, \end{aligned} \quad (30)$$

$$\begin{aligned} \|\nabla v_j\|_{L^2}^2 + \sum_{n=0}^{j-1} \|\nabla(v_{n+1} - v_n)\|_{L^2}^2 + \tau \sum_{n=0}^{j-1} \|\Delta v_{n+1}\|_{L^2}^2 \\ \leq \|\nabla v_0\|_{L^2}^2 + T \|I_0\|_{L^2}^2 + \tau \sum_{n=0}^{j-1} \|I_n\|_{L^2}^2, \end{aligned} \quad (31)$$

where C_P is the Poincaré constant. Note that, because of coupled system, we are not able to find the bound of v_n 's from (30) and (31). May be we need to combine with the estimates coming from (21) by choosing appropriate test

functions. Taking $\Psi = I_{n+1}$ in (21) and using (24), (29), and (30), we have

$$\begin{aligned}
& \|I_j\|_{L^2}^2 + \sum_{n=0}^{j-1} \|I_{n+1} - I_n\|_{L^2}^2 + 2\tau\nu \sum_{n=0}^{j-1} \|\nabla I_{n+1}\|_{L^2}^2 \\
& \leq \|I_0\|_{L^2}^2 + 2\tau \sum_{n=0}^{j-1} \|I_{n+1}\|_{L^2}^2 \\
& \quad + 2\tau \sum_{n=0}^{j-1} \left(\|v_0\|_{L^2}^2 + C_P^2 T \|I_0\|_{L^2}^2 + \tau C_P^2 \sum_{k=0}^n \|I_{k+1}\|_{L^2}^2 \right) \\
& \leq C_4 + C_5 \tau \sum_{k=0}^{j-1} \|I_{k+1}\|_{L^2}^2, \tag{32}
\end{aligned}$$

for some constants $C_4, C_5 > 0$, only depend on T, C_P, v_0, I_0 . We now apply discrete Gronwall's lemma (implicit form) and obtain the following: there exists $\tau_1 > 0$ such that for all time step sizes $0 < \tau < \tau_1$,

$$\max_{0 \leq j \leq N} \|I_j\|_{L^2}^2 + \sum_{n=0}^{N-1} \|I_{n+1} - I_n\|_{L^2}^2 + 2\tau\nu \sum_{n=0}^{N-1} \|\nabla I_{n+1}\|_{L^2}^2 \leq C_6, \tag{33}$$

where $C_6 > 0$ is independent of $\tau > 0$. We now use (33) in (30) and (31), and get

$$\max_{0 \leq j \leq N} \|v_j\|_{H^1}^2 + \sum_{n=0}^{N-1} \|v_{n+1} - v_n\|_{H^1}^2 + \tau \sum_{n=0}^{N-1} \left(\|\nabla v_{n+1}\|_{L^2}^2 + \|\Delta v_{n+1}\|_{L^2}^2 \right) \leq C_7, \tag{34}$$

for some constant $C_7 > 0$, independent of τ with $0 < \tau < \tau_1$. Again one may choose $\Psi = -\Delta I_{n+1}$ (formally) in (21) and use the integration by parts formula, (24), Cauchy-Schwarz and Young's inequalities, (29), (28), (34) and the fact that $\|\nabla g(u_n)\|_{L^\infty} \leq C(\xi, \Omega, k) \|u_n\|_{H^1}$ to get, after the application of discrete Gronwall's lemma (implicit form),

$$\max_{1 \leq j \leq N} \|\nabla I_j\|_{L^2}^2 + \sum_{n=0}^{N-1} \|\nabla(I_{n+1} - I_n)\|_{L^2}^2 + \tau \sum_{n=0}^{j-1} \|\Delta I_{n+1}\|_{L^2}^2 \leq C_8, \tag{35}$$

with $C_8 > 0$, independent of τ with $0 < \tau < \tau_2$ for some $\tau_2 > 0$. Note that, for $\tau_0 = \min\{\tau_1, \tau_2\}$, (33), (34) and (35) all hold true. Putting things together, we arrive at the following theorem.

Theorem 3.1 Let $I_0 \in H^1$. Then there exist constants $\tau_0 > 0$ and $C > 0$ such that for all time step sizes $\tau > 0$ with $0 < \tau < \tau_0$, there holds

$$\begin{aligned}
& \max_{1 \leq j \leq N} \left(\|u_j\|_{H^1}^2 + \|v_j\|_{H^1}^2 + \|I_j\|_{H^1}^2 \right) \\
& \quad + \sum_{n=0}^{N-1} \left(\|u_{n+1} - u_n\|_{H^1}^2 + \|v_{n+1} - v_n\|_{H^1}^2 + \|I_{n+1} - I_n\|_{H^1}^2 \right) \\
& \quad + \tau \sum_{n=0}^{N-1} \left(\|\Delta u_{n+1}\|_{L^2}^2 + \|\Delta v_{n+1}\|_{L^2}^2 + \|\Delta I_{n+1}\|_{L^2}^2 \right) \leq C, \tag{36}
\end{aligned}$$

where u_j, v_j and I_j solves (19), (20) and (21) respectively.

3.4 Continuation and existence of weak solution

Let $\{t_n\}_{n=0}^N$ be a uniform partition of $[0, T]$ with time-step size τ as described in Subsection 3.2. For any sequence $\{x_n\} \subset \mathbb{X}$, where \mathbb{X} is a Banach space, we define the difference quotient $d_t x_{n+1} = \frac{x_{n+1} - x_n}{\tau}$ for $0 \leq n \leq N-1$. The globally time interpolant $X_\tau \in C(\mathbb{X})$ of $\{x_n\}$ is defined via

$$X_\tau(t) := \frac{t - t_n}{\tau} x_{n+1} + \frac{t_{n+1} - t}{\tau} x_n, \quad \forall t \in (t_n, t_{n+1}].$$

Moreover, we define the piecewise constant in time interpolants $X_\tau^+(t)$ and $X_\tau^-(t)$ as follows:

$$X_\tau^+(t) := x_{n+1}, \quad X_\tau^-(t) := x_n, \quad \forall t \in (t_n, t_{n+1}],$$

with $x_{-1} = x_0$ and $x_{N+1} = 0$. With the above notation, we now show the boundedness of the sequence $\{\partial_t \mathcal{U}_\tau\}_{\tau>0}$ in $L^2(H^1(\Omega)')$. To do so, let $\Psi \in H^1(\Omega)' \setminus \{0\}$, and $t \in (t_n, t_{n+1}]$ where $0 \leq n \leq N-1$. Then from (19), we have, by using Cauchy-Schwarz inequality and (15),

$$\langle \partial_t \mathcal{U}_\tau, \Psi \rangle \leq \left(|\Omega|^{\frac{1}{2}} + \max_{0 \leq n \leq N-1} \|u_{n+1}\|_{H^1} \right) \|\Psi\|_{H^1}, \quad (37)$$

and hence, thanks to Theorem 3.1,

$$\|\partial_t \mathcal{U}_\tau\|_{L^2(H^1(\Omega)')}^2 \leq C \left(\tau \sum_{n=0}^{N-1} |\Omega| + T \max_{0 \leq n \leq N-1} \|u_{n+1}\|_{H^1}^2 \right) \leq C. \quad (38)$$

Similarly, the sequences $\{\partial_t \mathcal{V}_\tau\}_{\tau>0}$ and $\{\partial_t \mathcal{I}_\tau\}_{\tau>0}$ are bounded in $L^2(H^{-1}(\Omega))$ and $L^2(H^1(\Omega)')$ respectively. Moreover, there exists a constant $C > 0$ such that for all $0 < \tau < \tau_0$,

$$\|\partial_t \mathcal{V}_\tau\|_{L^2(H^{-1}(\Omega))}^2 + \|\partial_t \mathcal{I}_\tau\|_{L^2(H^1(\Omega)')}^2 \leq C. \quad (39)$$

Thanks to (38), (39) and Theorem 3.1, by using classical results of compact inclusion in Sobolev spaces [31], there exists $(I, u, v) \in W_1(0, T) \times W_1(0, T) \times W_2(0, T)$ such that along a subsequence (still we denote it by the same index) the following hold:

$$\begin{cases} \mathcal{I}_\tau^+, \mathcal{I}_\tau^- \rightharpoonup^* I & \text{in } L^\infty(H^1); \quad \partial_t \mathcal{I}_\tau \rightharpoonup \partial_t I & \text{in } L^2(H^1(\Omega)'), \\ \mathcal{I}_\tau, \mathcal{I}_\tau^\pm \rightharpoonup I & \text{in } L^2(H^1); \quad \mathcal{I}_\tau, \mathcal{I}_\tau^\pm \rightarrow I & \text{in } L^2(L^2), \\ |\nabla G_\xi * \mathcal{I}_\tau^-|^2 \rightarrow |\nabla G_\xi * I|^2 & \text{in } L^2(L^2) \text{ and a.e. } (0, T) \times \Omega, \\ h(|\nabla G_\xi * \mathcal{I}_\tau^-|^2) \rightarrow h(|\nabla G_\xi * I|^2) & \text{in } L^2(L^2), \\ \mathcal{U}_\tau^+, \mathcal{U}_\tau^- \rightharpoonup^* u & \text{in } L^\infty(H^1); \quad \partial_t \mathcal{U}_\tau \rightharpoonup \partial_t u & \text{in } L^2(H^1(\Omega)'), \\ \mathcal{U}_\tau, \mathcal{U}_\tau^\pm \rightharpoonup u & \text{in } L^2(H^1); \quad \mathcal{U}_\tau, \mathcal{U}_\tau^\pm \rightarrow u & \text{in } L^2(L^2), \\ g(\mathcal{U}_\tau^+) \rightarrow g(u) & \text{in } L^2(L^2), \\ \mathcal{V}_\tau^+, \mathcal{V}_\tau^- \rightharpoonup^* v & \text{in } L^\infty(H_0^1); \quad \partial_t \mathcal{V}_\tau \rightharpoonup \partial_t v & \text{in } L^2(H^{-1}(\Omega)), \\ \mathcal{V}_\tau, \mathcal{V}_\tau^\pm \rightharpoonup v & \text{in } L^2(H_0^1); \quad \mathcal{V}_\tau, \mathcal{V}_\tau^\pm \rightarrow v & \text{in } L^2(L^2). \end{cases} \quad (\tau \rightarrow 0), \quad (40)$$

For any $\Psi \in H^1$ and $\Phi \in H_0^1$, we rewrite (19), (20) and (21) in terms of $\mathcal{U}_\tau, \mathcal{U}_\tau^+, \mathcal{U}_\tau^-, \mathcal{V}_\tau, \mathcal{V}_\tau^+, \mathcal{V}_\tau^-, \mathcal{I}_\tau, \mathcal{I}_\tau^+$, and \mathcal{I}_τ^- , integrate with respect to the time variable and make use of (40) to pass to the limit as $\tau \rightarrow 0$ in the resulting variational formulation to arrive at (16), (17) and (18). In other words, the triple (I, u, v) is a weak solution of (10)-(13).

3.5 Uniqueness of weak solution

We use standard methodology [32] to prove the uniqueness of weak solution of (10)-(13). Let (I_1, u_1, v_1) and (I_2, u_2, v_2) be two sets of solution for the system (10)-(13) with $I_1 \neq I_2$, $u_1 \neq u_2$ and $v_1 \neq v_2$. Let $\tilde{I} := I_1 - I_2$, $\tilde{U} := u_1 - u_2$, $\tilde{V} := v_1 - v_2$ and $g_i = g(u_i)$ ($i = 1, 2$). Then, the following equations hold in the sense of distribution:

$$\frac{\partial \tilde{I}}{\partial t} - \nabla(g_1 \nabla \tilde{I}) = \nabla((g_1 - g_2) \nabla I_2) - 2\tilde{V}, \quad \text{in } \Omega_T, \quad (41)$$

$$\frac{\partial \tilde{U}}{\partial t} - \Delta \tilde{U} = \left(h(|\nabla G_\xi * I_1|^2) - h(|\nabla G_\xi * I_2|^2) \right) - \tilde{U}, \quad \text{in } \Omega_T, \quad (42)$$

$$\frac{\partial \tilde{V}}{\partial t} - \Delta \tilde{V} = \tilde{I}, \quad \text{in } \Omega_T, \quad (43)$$

$$\tilde{I}(0, x) = 0 = \tilde{U}(0, x) = \tilde{V}(0, x), \quad \text{in } \Omega. \quad (44)$$

Note that

$$\nu_1 := \frac{1}{1 + \frac{C \|u_1\|_{L^\infty(H^1)}}{k^2}} \leq g(u_1); \quad \|(g_1 - g_2)\|_{L^\infty} \leq C_\xi \|(u_1 - u_2)\|_{L^2}.$$

Similar to a-priori estimates, we have for a.e. $t \in (0, T)$ with $\tilde{C}_I := \|\nabla I\|_{L^\infty(L^2)}^2$,

$$\begin{aligned} \frac{1}{2} \frac{d}{dt} \|\tilde{I}\|_{L^2}^2 &\leq \tilde{C}_I C(\nu_1) \|(g_1 - g_2)\|_{L^\infty}^2 + \|\tilde{I}\|_{L^2}^2 + \|\tilde{V}\|_{L^2}^2 \\ &\leq \tilde{C} \|\tilde{U}\|_{L^2}^2 + \|\tilde{I}\|_{L^2}^2 + \|\tilde{V}\|_{L^2}^2. \end{aligned} \quad (45)$$

Similarly, by multiplying (42) by \tilde{U} and integrating over Ω , we get

$$\frac{d}{dt} \|\tilde{U}\|_{L^2}^2 + 2\|\nabla \tilde{U}\|_{L^2}^2 \leq C \|h(|\nabla G_\xi * I_1|^2) - h(|\nabla G_\xi * I_2|^2)\|_{L^2}^2 + \|\tilde{U}\|_{L^2}^2. \quad (46)$$

By using Lipschitz continuity of h along with Gagliardo-Nirenberg inequality, we have

$$\|h(|\nabla G_\xi * I_1|^2) - h(|\nabla G_\xi * I_2|^2)\|_{L^2}^2 \leq C(c_h, \xi, I_1, I_2) \|\tilde{I}\|_{L^2}^2, \quad (47)$$

and hence

$$\frac{d}{dt} \|\tilde{U}\|_{L^2}^2 \leq C \|\tilde{I}\|_{L^2}^2. \quad (48)$$

In a similar way, one can easily deduce that

$$\frac{d}{dt} \|\tilde{V}\|_{L^2}^2 \leq C \left(\|\tilde{I}\|_{L^2}^2 + \|\tilde{V}\|_{L^2}^2 \right). \quad (49)$$

We now add (45)-(49) and then apply Gronwall's inequality to infer that $\tilde{I} \equiv 0$, $\tilde{U} \equiv 0$ and $\tilde{V} \equiv 0$. In other words, weak solution of the proposed model (10)-(13) is unique.

4 Numerical Approximation

In this section, we discuss the numerical implementation of the proposed model (10)-(13). To solve the model numerically, we have applied the generalized weighted average finite difference scheme which has a combined nature of the forward Euler method and the backward Euler method, at n^{th} and $(n+1)^{\text{th}}$ step, respectively. The image variable I , edge variable u and fidelity term v are calculated at each iteration.

In the derivation of finite difference formulas, h and τ are considered as spatial step size and time step size, respectively. Let $I(x_i, y_j, t_n)$ express the gray level of the image plane $I_{i,j}^n$, where $x_i = ih, y_j = jh$ and $t_n = n\tau$. Also, we consider $v_{i,j}^0 = 0$ and $u_{i,j}^0 = G_\xi * |\nabla I_{i,j}^0|^2$. Derivatives are approximated by central difference formula as,

$$\begin{aligned} \frac{\partial I}{\partial x} &\approx \frac{I_{i+1,j}^n - I_{i-1,j}^n}{2h}, \quad \frac{\partial I}{\partial y} \approx \frac{I_{i,j+1}^n - I_{i,j-1}^n}{2h}, \\ \frac{\partial^2 I}{\partial^2 x} &\approx \frac{I_{i+1,j}^n - 2I_{i,j}^n + I_{i-1,j}^n}{h^2}, \quad \frac{\partial^2 I}{\partial^2 y} \approx \frac{I_{i,j+1}^n - 2I_{i,j}^n + I_{i,j-1}^n}{h^2}. \end{aligned}$$

The discrete form of (10)-(13) can be written as;

$$I_{i,j}^{n+1} - \frac{\tau}{2} ((\nabla(g(u)\nabla I)_{i,j}^{n+1} - 2\lambda v_{i,j}^{n+1})) = I_{i,j}^n + \frac{\tau}{2} ((\nabla(g(u)\nabla I)_{i,j}^n - 2\lambda v_{i,j}^n)), \quad (50)$$

$$\frac{u_{i,j}^{n+1} - u_{i,j}^n}{\tau} = \varphi \left(h(|\nabla I_{\xi_{i,j}}^n|^2) - u_{i,j}^{n+1} + \frac{\psi^2}{2} \Delta u_{i,j}^{n+1} \right), \quad (51)$$

$$\frac{v_{i,j}^{n+1} - v_{i,j}^n}{\tau} = \Delta v_{i,j}^{n+1} - (I_{i,j}^n - I_{i,j}^0), \quad (52)$$

where,

$$\Delta w_{i,j}^n = \frac{w_{i+1,j}^n - 2w_{i,j}^n + w_{i-1,j}^n}{h^2} + \frac{w_{i,j+1}^n - 2w_{i,j}^n + w_{i,j-1}^n}{h^2}, \quad (53)$$

for $w = u, v$. Moreover the diffusion term in (10)-(13) approximated using the central difference scheme as,

$$\begin{aligned} \nabla(g(u)\nabla I)_{i,j} &= \frac{1}{h^2} (g_{i+\frac{1}{2},j} (I_{i+1,j} - I_{i,j}) - g_{i-\frac{1}{2},j} (I_{i,j} - I_{i-1,j})) + \\ &\quad g_{i,j+\frac{1}{2}} (I_{i,j+1} - I_{i,j}) - g_{i,j-\frac{1}{2}} (I_{i,j} - I_{i,j-1}), \end{aligned} \quad (54)$$

with the Neumann boundary conditions:

$$\begin{aligned} I_{i,0} - I_{i,1} &= 0, & I_{i,N-1} - I_{i,N} &= 0, & \text{for } 0 \leq i \leq M, \\ I_{0,j} - I_{1,j} &= 0, & I_{M-1,j} - I_{M,j} &= 0, & \text{for } 0 \leq j \leq N. \end{aligned}$$

Further, to solve the algebraic system of the the form $AI^{n+1} = B$, generated from numerical discretization, hybrid Bi-Conjugate Gradient Stabilized solver has been used [33, 37].

Apart from the numerical discretization of (10)-(13), a stopping criterion is needed to terminate the diffusion process. To achieve this goal, we start with an initial image I_0 and apply the system (10)-(13) repeatedly. This results in a family of smoother images $I(t, x); t > 0$, which depicts refined versions of I_0 . After sufficient iterations, changes between two consecutive iterations become redundant. At this point, the convergence of the iterative procedure has been achieved. Now, we use the following measure as a stopping criterion,

$$\frac{\|I^{k+1} - I^k\|_2^2}{\|I^k\|_2^2} \leq \varepsilon. \quad (55)$$

Here, we use $\varepsilon = 10^{-4}$ as a fixed threshold. I^k and $I^{(k+1)}$ depict the image planes at the k^{th} and $(k+1)^{th}$ iteration, respectively. Parameter values used for the numerical experiments are mentioned in the caption of each figure. For

Algorithm 1 Algorithm of CPDE model for Image Denoising

- 1: Inputs: $I^{(0)} = I_0$ as initial solution or initial noisy image,
 $v^{(0)} = 0$ as initial edge variable and $u^{(0)} = G_\xi * |\nabla I^{(0)}|^2$, τ as time step, $k = 0$.
- 2: Result: Denoised image (I)
- 3: Calculate $I^{(k+1)}$, $u^{(k+1)}$ and $v^{(k+1)}$ from

$$\begin{bmatrix} 1 - \frac{\tau}{2}A(I^{k+1}) & 0 & \tau\lambda \\ 0 & 1 + \tau(1 - \frac{\psi^2}{2}\Delta) & 0 \\ 0 & 0 & 1 - \tau\Delta \end{bmatrix} \begin{bmatrix} I^{k+1} \\ u^{k+1} \\ v^{k+1} \end{bmatrix} = \begin{bmatrix} I^k + \frac{\tau}{2}(A(I^k) - 2\lambda v^k) \\ u^k + \tau\varphi h(\|\nabla I_\xi^k\|^2) \\ v^k - \tau(I^k - I^0) \end{bmatrix}$$

- 4: Solve the algebraic system (obtained using step 3), using Hybrid BiCGStab solver .
- 5: Check if

$$\frac{\|I^{k+1} - I^k\|_2^2}{\|I^k\|_2^2} \leq \varepsilon = 10^{-4}$$

then stop or go to Step 3.

- 6: end
-

the TV and NLM model, we have reproduced the results by utilizing the fact as mention in [19] and [39] respectively. Apart from the parameters displayed in the captions, we have chosen $\varphi = 1$ and $\xi = 1$ for the present model and a uniform time step size $\tau = 0.1$ for the current as well as the other discussed approaches.

5 Results and Discussion

The proposed CPDE model was employed using the finite difference scheme given in the previous section. Image denoising using (10)-(13) was compared with the results of other state-of-art models available in the literature. Especially, TV model [19], NS model [27], Luo model [26], RD model [25], PV model [28], SYS model [38] are considered for the comparison. Apart from the diffusion-based approaches, non-iterative approach (Non-Local Means method) [39] is also used for comparison with the present method. Since the space-time regularization based proposed model is claimed to be an improvement over the existing CPDE models, our main aim was to compare the edge detection and denoising results with these models (NS Model, and Luo model). In this process, the considered non-linear diffusion models are solved by the existing numerical schemes. And also, to stop the iterative process of each smoothing algorithm discussed stopping criteria equation (55) is employed. The effectiveness of results was evaluated through several standard gray level test images which are degraded with additive Gaussian noise of zero mean and different levels of standard deviations. We have artificially added additive Gaussian noise of different standard deviations ranging from 20 to 50 by using our MATLAB program. Also, to evaluate the efficiency of our model, quantitative comparisons in terms of Peak signal to noise ratio (PSNR)[2], mean structural similarity index measure (MSSIM)[40], Gradient of peak signal to noise ratio (PSNR_{Grad})[41], Improvement in signal to noise ratio (ISNR)[2] have been shown with existing models. A higher value of quantity metrics suggests that the filtered image is closer to the noise-free image.

(a). Peak signal to noise ratio (PSNR)[2] can measure the match between the clean (I) and denoised image (\hat{I}),

$$\text{PSNR}(I, \hat{I}) = 10 \log_{10} \frac{\text{MN} |\max(I) - \min(I)|^2}{\|\hat{I} - I\|_{L^2}^2}.$$

(b). In addition to PSNR, gradient of peak signal to noise ratio ($\text{PSNR}_{\text{Grad}}$) is also used to measure the match between the derivatives of reconstructed and true image, defined as

$$\text{PSNR}_{\text{Grad}} = \frac{1}{2} (\text{PSNR}(I_x, \hat{I}_x) + \text{PSNR}(I_y, \hat{I}_y)),$$

where (I_x, I_y) and (\hat{I}_x, \hat{I}_y) are the derivatives of ground truth image (I) and denoised image (\hat{I}).

(c). Structural similarity index (SSIM) [40], is used to calculate the similarity between structure of clean and reconstructed images, and can be given as,

$$\text{SSIM}(X, Y) = \frac{(2\mu_x\mu_y + c_1)(2\sigma_{xy} + c_2)}{(\mu_x^2 + \mu_y^2 + c_1)(\sigma_x^2 + \sigma_y^2 + c_2)},$$

here $\mu_x, \mu_y, \sigma_x^2, \sigma_y^2, \sigma_{xy}$ are the average, variance and covariance of X and Y , respectively. The variables c_1 and c_2 are used to stabilize the division with weak denominator. To find overall performance of the image, we used a mean SSIM index (MSSIM),

$$\text{MSSIM}(X, Y) = \frac{1}{N} \sum_{i=1}^N \text{SSIM}(X_i, Y_i),$$

where X and Y are used to represent the original and the denoised images, respectively. N is the number of local windows in the image, and X_i and Y_i are the image contents at the i^{th} local window.

(d). Improvement in signal to noise ratio (ISNR) [2], is simply the difference between the improved and the original signal to noise ratio,

$$\text{ISNR} = 10 \log_{10} \left(\frac{\sum_{i=1}^M \sum_{j=1}^N (I - I_0)^2}{\sum_{i=1}^M \sum_{j=1}^N (I - I_t)^2} \right).$$

To test the effectiveness of the proposed model, figure[1] presents the denoising results for Walkbridge test image that contain additive Gaussian noise of $\sigma = 40$, which make the features hard to visualize. The restored outputs obtained from the state-of-the-art diffusion models depict that the denoised images are not satisfactory and the texture information of the image is ruined. From the figure[1e], it is easy to perceive that the proposed model can effectively eliminate all noise particles and preserve the original structure of the image.

Further, to showcase the efficiency of our model, in figure 2, we compare the visual quality of the mosaic image computed by the present model along with the other existing models. Here we present the denoised images and 3D surface plots of the denoised images side by side for better comparison. From the figure, it can be observed that our model works better in terms of noise removal as compared to other models. From the 3D surface plots of the denoised images, one can see that our model leave fewer fluctuations with compare to the other models, it indicates that the proposed model not only removes noise efficiently but also preserves the fine structure as compared to the other models.

To further confirm the ability of the proposed model, in figure[3], we present the comparison of the denoised Pirate image which was initially degraded with additive Gaussian noise with very low SNR value 3.70. From figure[3], it is clear that the proposed algorithm retains more texture information in addition to noise reduction, which makes our filtered image better in comparison to other models considered here.

Along with the qualitative analysis using full image surface, we also study the quality of the resultant images considering a slice of the Boat image and the Livingroom image with different noise levels. Figure 4 shows the signals of the original, noisy and restored images obtained by the proposed CPDE model and other discussed CPDE models. From these figures, it is easy to conclude that the restored signals computed by the proposed model are more closure to the clean signals in comparison to other discussed models.

In addition to qualitative comparisons, the quantitative results, in terms of PSNR and MSSIM values for different test images as well as noise levels ($\sigma = 20, 30, 40, 50$), are shown in tables [1]-[4]. To ease the comparison, the highest

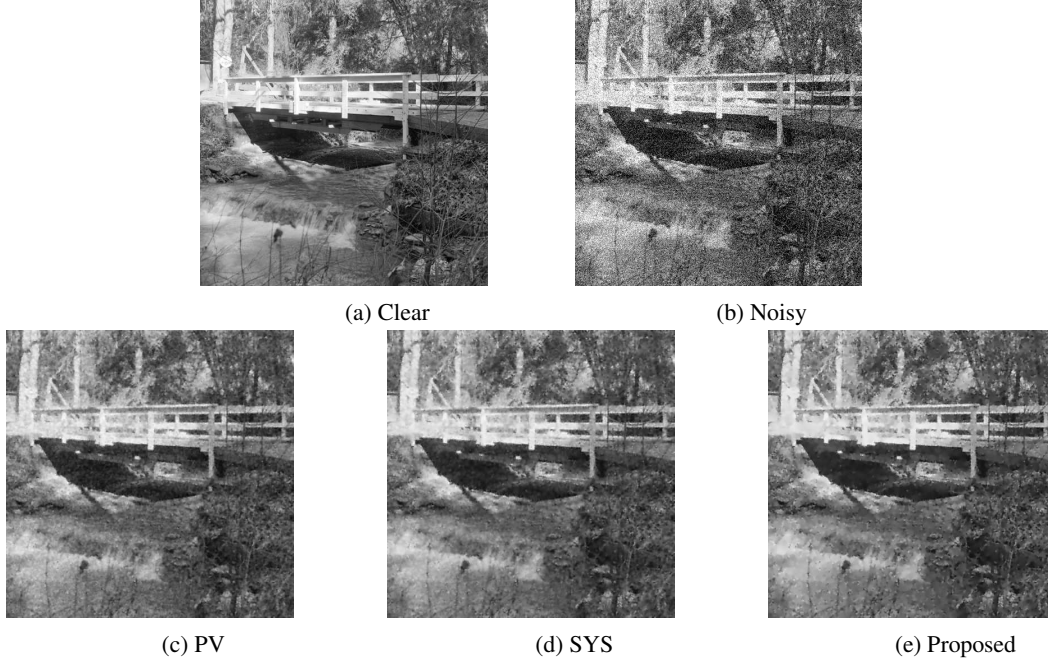


Figure 1: (a) Clear image; (b) Noisy image with Gaussian noise of mean 0.0 and $\sigma = 40$; Denoised image using (c) PV Model, $\lambda = 0.01, K = 8$; (d) SYS Model, $\lambda = 4, K = 8$; (e) Proposed model, $\psi = 0.1, k = 4.45$.

Table 1: Comparison of MSSIM and PSNR values for various approaches and proposed model. Clean image is degraded by additive Gaussian noise of mean 0.0 and $\sigma = 20$.

Images	Measure	TV[19]	NS[27]	Luo[26]	RD[25]	NLM[39]	PV[28]	SYS[38]	Proposed
Boat	MSSIM	0.8232	0.8883	0.8774	0.8886	0.9105	0.8900	0.8943	0.9219
	PSNR	28.10	28.81	29.40	29.61	30.21	29.69	29.84	30.24
Lake	MSSIM	0.8539	0.8996	0.8775	0.8788	0.9140	0.9060	0.9074	0.9268
	PSNR	28.37	28.07	28.65	28.61	29.27	28.87	29.08	29.57
Livingroom	MSSIM	0.8790	0.8698	0.8855	0.8849	0.8870	0.8903	0.8912	0.9019
	PSNR	28.51	28.62	28.68	28.80	29.11	28.87	28.93	29.22
Mandrill	MSSIM	0.8958	0.9001	0.8909	0.8997	0.8684	0.9015	0.9029	0.9034
	PSNR	27.51	27.71	27.77	27.95	27.62	28.24	28.37	28.46
Pirate	MSSIM	0.8615	0.9053	0.8764	0.8714	0.8908	0.8936	0.8943	0.9055
	PSNR	28.54	29.40	29.20	29.07	29.69	29.51	29.53	29.90
Walkbridge	MSSI	0.9077	0.9141	0.9070	0.9101	0.8747	0.9093	0.9089	0.9143
	PSNR	26.79	26.83	27.05	26.99	26.72	26.99	27.02	27.24
Woman	MSSIM	0.8007	0.9191	0.8257	0.8206	0.9243	0.9262	0.9225	0.9396
	PSNR	30.35	33.83	31.31	31.29	33.64	34.47	34.59	35.03
Mosaic	MSSIM	0.9699	0.9091	0.9270	0.9600	0.9588	0.9675	0.9290	0.9780
	PSNR	34.28	32.71	33.66	34.44	34.12	33.38	32.54	34.74

Table 2: Comparison of MSSIM and PSNR values for various approaches and proposed model. Clean image is degraded by additive Gaussian noise of mean 0.0 and $\sigma = 30$.

Images	Measure	TV[19]	NS[27]	Luo[26]	RD[25]	NLM[39]	PV[28]	SYS[38]	Proposed
Boat	MSSIM	0.7157	0.6923	0.7324	0.7327	0.8568	0.8360	0.8400	0.8841
	PSNR	25.28	25.71	25.83	26.01	28.02	27.79	27.96	28.47
Lake	MSSIM	0.7644	0.7676	0.7751	0.7820	0.8705	0.8576	0.8637	0.8956
	PSNR	25.27	25.41	25.72	26.01	27.38	27.12	27.33	27.87
Livingroom	MSSIM	0.7859	0.8510	0.7922	0.7969	0.8229	0.8273	0.8321	0.8515
	PSNR	25.91	27.28	26.14	26.40	26.90	26.97	27.02	27.39
Mandrill	MSSIM	0.8188	0.7633	0.8262	0.8268	0.7873	0.8309	0.8395	0.8454
	PSNR	24.94	25.46	25.55	25.52	25.43	26.13	26.27	26.47
Pirate	MSSIM	0.7745	0.8348	0.7765	0.7905	0.8346	0.8392	0.8400	0.8575
	PSNR	26.18	27.05	26.26	26.86	27.72	27.86	27.81	28.20
Walkbridge	MSSIM	0.8391	0.8194	0.8431	0.8453	0.8015	0.8462	0.8508	0.8566
	PSNR	24.60	24.07	24.91	24.99	24.96	25.19	25.22	25.47
Woman	MSSIM	0.6834	0.8559	0.6805	0.7108	0.8861	0.8963	0.8922	0.9200
	PSNR	27.58	31.16	27.47	28.58	31.38	32.58	32.64	33.25
Mosaic	MSSIM	0.9558	0.8827	0.8800	0.9467	0.9477	0.9520	0.8764	0.9659
	PSNR	31.63	30.38	30.68	31.65	31.69	31.10	30.24	31.97

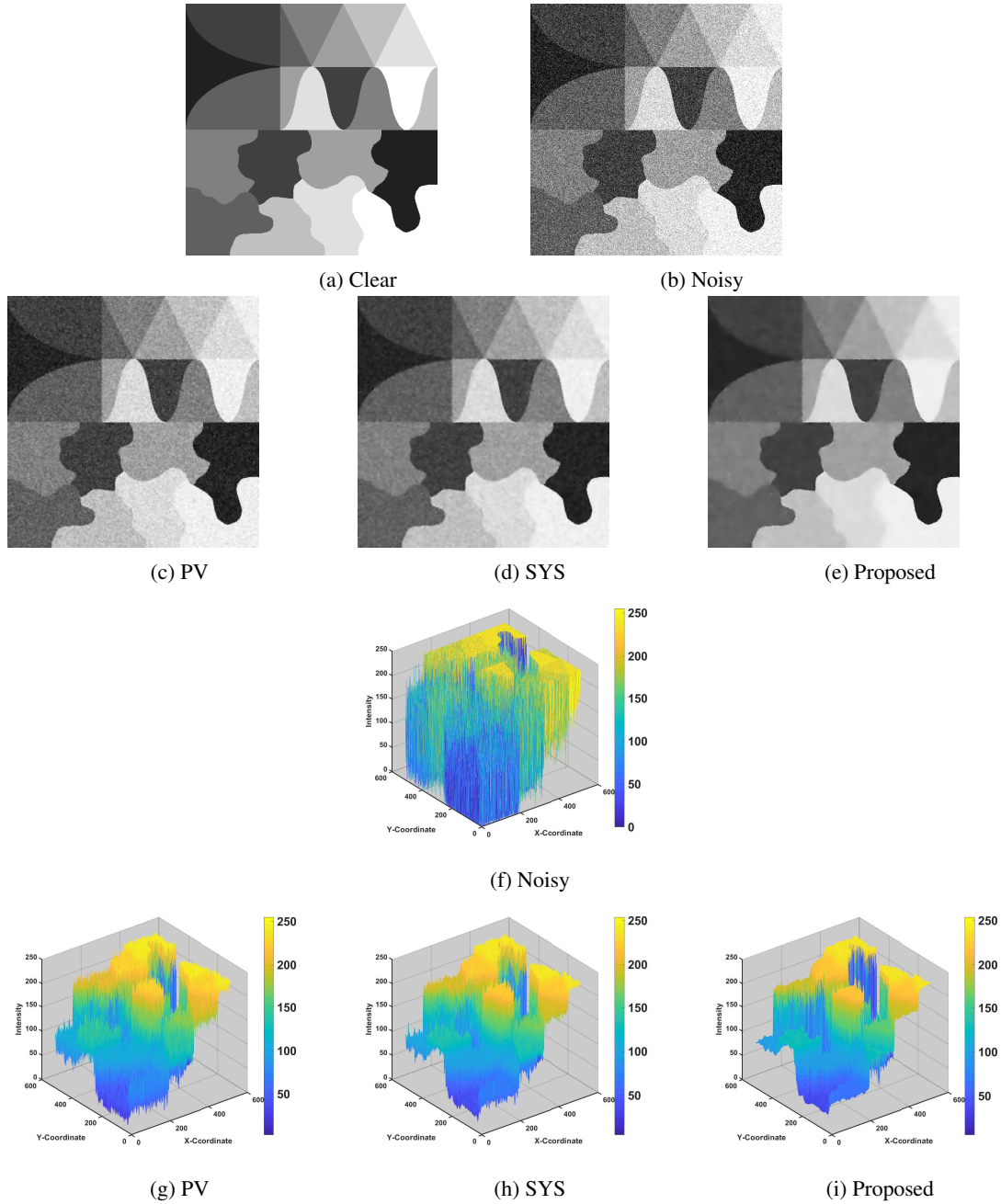


Figure 2: (a) Clear image (b) Noisy image with Gaussian noise of mean 0.0 and s.d. 40 (c) PV Model, $\lambda = 0.01$, $K = 1$; (d) SYS Model, $\lambda = 0.1$, $K = 4$; (e) Proposed Model, $\psi = 1$, $k = 3.75$. (f-i) 3D surfaces of images

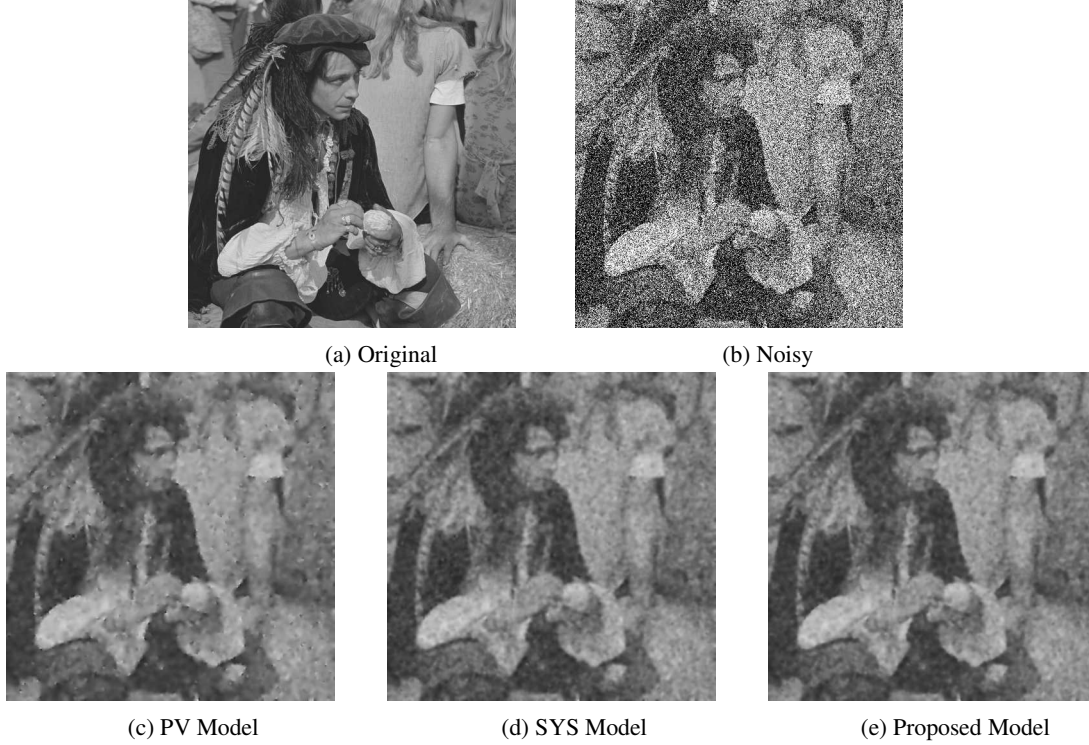


Figure 3: (a) Clear image (b)Heavily noisy image with low SNR=3.70; Improved SNR values by different models: (c) SNR=15.41; $\lambda = 0.01, K = 11$ (d) SNR=15.37; $\lambda = 1, K = 10$ (e) SNR=15.53; $\psi = 1, k = 14$.

Table 3: Comparison of MSSIM and PSNR values for various approaches and proposed model. Clean image is degraded by additive Gaussian noise of mean 0.0 and $\sigma = 40$.

Images	Measure	TV[19]	NS[27]	Luo[26]	RD[25]	NLM[39]	PV[28]	SYS[38]	Proposed
Boat	MSSIM	0.6305	0.6146	0.6290	0.6481	0.8022	0.7862	0.7798	0.8470
	PSNR	23.43	23.41	23.35	24.19	26.40	26.51	26.60	27.21
Lake	MSSIM	0.6964	0.7052	0.6927	0.7117	0.8245	0.8154	0.8173	0.8644
	PSNR	23.67	23.70	23.62	24.33	25.93	25.94	26.05	26.62
Livingroom	MSSIM	0.6941	0.6989	0.6855	0.7095	0.7600	0.7699	0.7731	0.7991
	PSNR	23.85	23.36	23.56	24.50	25.37	25.68	25.70	26.11
Mandrill	MSSIM	0.7409	0.7456	0.7462	0.7525	0.7164	0.7692	0.7777	0.7844
	PSNR	23.14	23.24	23.41	23.82	24.01	24.75	24.90	25.10
Pirate	MSSIM	0.6882	0.6913	0.6800	0.7067	0.7849	0.7869	0.7870	0.8132
	PSNR	24.32	24.23	24.04	25.06	26.35	26.64	26.58	27.06
Walkbridge	MSSIM	0.7728	0.7883	0.7722	0.7821	0.7371	0.7922	0.7944	0.7985
	PSNR	23.05	23.48	23.08	23.54	23.76	24.01	24.05	24.24
Woman	MSSIM	0.5976	0.7317	0.5671	0.6235	0.8513	0.8690	0.8641	0.9037
	PSNR	25.75	27.59	25.93	26.61	29.75	31.00	30.96	31.65
Mosaic	MSSIM	0.9384	0.8892	0.8315	0.9328	0.9388	0.9303	0.8373	0.9508
	PSNR	29.43	28.51	28.38	29.46	29.66	29.04	28.15	29.77

Table 4: Comparison of MSSIM and PSNR values for various approaches and proposed model. Clean image is degraded by additive Gaussian noise of mean 0.0 and $\sigma = 50$.

Images	Measure	TV [19]	NS [27]	Luo [26]	RD [25]	NLM[39]	PV[28]	SYS[38]	Proposed
Boat	MSSIM	0.5648	0.5793	0.5519	0.5813	0.7523	0.7425	0.7333	0.8159
	PSNR	22.02	21.70	21.50	22.75	25.14	25.48	25.46	26.16
Lake	MSSIM	0.6404	0.6657	0.6232	0.6540	0.7828	0.7747	0.7710	0.8334
	PSNR	22.47	22.09	21.98	23.06	24.75	24.89	24.94	25.53
Livingroom	MSSIM	0.6265	0.6424	0.5981	0.6429	0.7090	0.7245	0.7229	0.7562
	PSNR	22.51	21.57	21.54	23.17	24.28	24.75	24.72	25.17
Mandrill	MSSIM	0.6707	0.6177	0.6765	0.6846	0.6505	0.7102	0.7173	0.7261
	PSNR	21.77	21.48	22.06	22.49	22.99	23.69	23.87	24.06
Pirate	MSSIM	0.6275	0.6486	0.5969	0.6450	0.7423	0.7483	0.7454	0.7762
	PSNR	23.11	21.66	22.15	23.78	25.24	25.68	25.60	26.10
Walkbridge	MSSIM	0.7150	0.7046	0.7025	0.7243	0.6838	0.7414	0.7428	0.7483
	PSNR	22.00	21.75	21.52	22.44	22.84	23.10	23.16	23.34
Woman	MSSIM	0.5318	0.5702	0.5626	0.6143	0.8150	0.8430	0.8354	0.8830
	PSNR	24.30	22.02	22.56	25.02	28.23	29.31	29.25	29.81
Mosaic	MSSIM	0.9203	0.8404	0.8662	0.9189	0.9144	0.9078	0.7730	0.9333
	PSNR	27.61	26.93	26.55	27.66	27.71	27.34	26.51	27.87

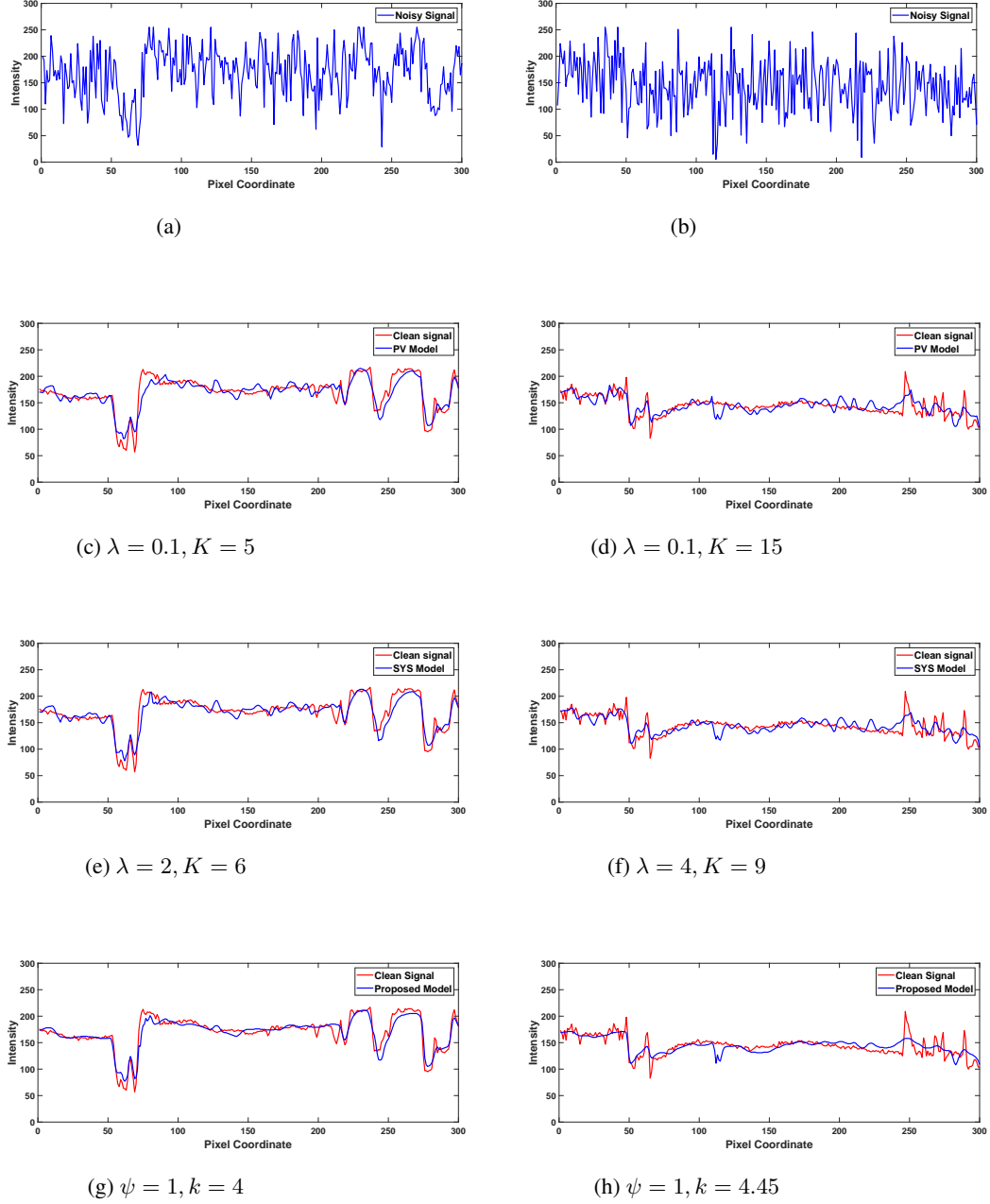


Figure 4: (a) The 219th slice of Boat image corrupted with Gaussian noise of mean 0.0 and $\sigma = 40$; (b) The 95th slice of Livingroom image corrupted with additive Gaussian noise of mean 0.0 and $\sigma = 50$; denoised using (c-d) PV model; (e-f) SYS model, and (g-h) Proposed model.

Table 5: Comparison of ISNR and PSNR_{grad} values for various approaches and proposed model. Clean image is degraded by additive Gaussian noise of mean 0.0 and $\sigma = 40$.

Images	Measure	TV[19]	NS[27]	Luo[26]	RD[25]	NLM[39]	PV[28]	SYS[38]	Proposed
Boat	ISNR	7.02	7.01	6.93	7.78	9.90	9.99	10.19	10.80
	PSNR _{grad}	27.04	27.01	26.86	28.07	30.84	30.90	31.28	31.64
Lake	ISNR	7.05	7.12	7.00	7.71	9.12	9.19	9.43	10.00
	PSNR _{grad}	27.23	27.30	27.12	28.05	30.11	30.19	30.21	30.62
Livingroom	ISNR	7.51	7.02	7.22	8.16	9.03	9.20	9.36	9.77
	PSNR _{grad}	27.68	27.33	27.51	28.62	29.84	30.04	30.25	30.62
Mandrill	ISNR	7.12	7.19	7.31	7.58	7.77	8.51	8.66	8.86
	PSNR _{grad}	26.59	26.70	26.83	27.44	27.91	28.48	28.58	28.88
Pirate	ISNR	7.92	7.83	7.64	8.66	9.96	10.14	9.99	10.66
	PSNR _{grad}	28.11	27.57	27.41	29.14	30.59	30.62	30.60	31.26
Walkbridge	ISNR	6.59	6.88	6.62	7.07	7.30	7.55	7.59	7.78
	PSNR _{grad}	26.55	26.65	26.59	27.14	27.68	27.71	27.73	27.98
Woman	ISNR	9.11	10.95	9.29	9.97	13.11	13.94	13.87	15.01
	PSNR _{grad}	30.05	32.36	30.72	31.46	34.77	37.37	37.30	38.80
Mosaic	ISNR	12.57	11.64	11.51	12.60	12.74	12.17	11.29	12.86
	PSNR _{grad}	37.34	35.68	35.48	37.37	37.52	36.01	34.92	37.56

values of both MSSIM and PSNR measures are highlighted in each table. The highest values of PSNR and MSSIM for each image, clearly shows that the proposed model is better than all other models considered in the table. We have a significant observation that proposed model performs better for higher noise densities, as can be seen from tables[3]-[4]. For low noise densities, such as $\sigma = 20$, our results are still batter or very closed to the best values. Hence, analysis of the results presented in the tables, reveals that the performance of the present model increases with increasing noise density. In table [5], apart from the MSSIM and PSNR, we show the quantitative comparison with gradient PSNR and ISNR values of the proposed model and the alternative approaches. Finally, we note that the different quantitative measures (in terms of PSNR, MSSIM, gradient PSNR, and ISNR values) confirm the superiority of the proposed approach in comparison with other models. Our comparison study shows that the proposed CPDE model preserves image structure efficiently in comparison to other earlier reported methods when signal-to-noise ratio is low. On the other hand, when signal-to-noise ratio is high, the present model restores image structure better than the other existing models. From the above discussion, it is confirmed that the proposed model is robust and more efficient than the available techniques considered here.

6 Conclusion

In this work, we propose a new CPDE based denoising framework. The proposed space-time regularization based image denoising approach highlights the choice of diffusion function and data fidelity term. For this purpose, we use the evolution equations to determine both the terms in the proposed model. It may be treated as the non-linear diffusion model which yield two separate PDEs to remove the noise with preservation of significant edges and fine structures. First, we establish the well-posedness of the proposed model using a time discretization method. Then, to solve the proposed model numerically, an implicit finite difference scheme along with advanced iterative solver has been used. We validate our model with different standard test images. Experimental studies confirm that the proposed model is more efficient than the existing models, in terms of quantitative measures and visual quality. Especially, the present model produces best results for high noise levels. We believe that present model has multidimensional applications which will ultimately benefit the society.

Competing interests

The authors declare that they have no competing interests.

Acknowledgments

Authors sincerely acknowledge Dr. Arnav Bhavsar, School of Computing and Electrical Engineering, Indian Institute of Technology Mandi, Himachal Pradesh, India for some valuable discussions and suggestions during the preparation of this manuscript.

References

- [1] L. Alvarez, F. Guichard, P.-L. Lions, J.-M. Morel, Axioms and fundamental equations of image processing, *Archive for rational mechanics and analysis* 123 (3) (1993) 199-257.
- [2] R. C. Gonzalez, R. E. Woods, *Digital image processing* (2002).
- [3] G. Aubert, P. Kornprobst, *Mathematical problems in image processing: partial differential equations and the calculus of variations*, Vol. 147, Springer, 2006.
- [4] K. Mikula, Image processing with partial differential equations, in: *Modern methods in scientific computing and applications*, Springer, 2002, pp. 283-321.
- [5] J. Nolen, *Partial differential equations and diffusion processes*, Tech. rep., Technical report, Stanford University. Department of Mathematics (2009).
- [6] J. Weickert, *Anisotropic diffusion in image processing*, Vol. 1, Teubner Stuttgart, 1998.
- [7] J. Weickert, Applications of nonlinear diffusion in image processing and computer vision, *Acta Math. Univ. Comenianae* 70 (1) (2001) 33-50.
- [8] A. P. Witkin, Scale-space filtering: A new approach to multi-scale description, in: *Acoustics, Speech, and Signal Processing, IEEE International Conference on ICASSP'84.*, Vol. 9, IEEE, 1984, pp. 150-153.
- [9] F. Catté, P.-L. Lions, J.-M. Morel, T. Coll, Image selective smoothing and edge detection by nonlinear diffusion, *SIAM Journal on Numerical analysis* 29 (1) (1992) 182-193.
- [10] P. Perona, J. Malik, Scale-space and edge detection using anisotropic diffusion, *Pattern Analysis and Machine Intelligence, IEEE Transactions on* 12 (7) (1990) 629-639.
- [11] J. Weickert, A review of nonlinear diffusion filtering, in: *Scale-space theory in computer vision*, Springer, 1997, pp. 1-28.
- [12] X. Liu, L. Huang, Z. Guo, Adaptive fourth-order partial differential equation filter for image denoising, *Applied Mathematics Letters* 24 (8) (2011) 1282-1288.
- [13] A. Siddig, Z. Guo, Z. Zhou, B. Wu, An image denoising model based on a fourth-order nonlinear partial differential equation, *Computers & Mathematics with Applications* 76 (5) (2018) 1056-1074.
- [14] Y.-L. You, M. Kaveh, Fourth-order partial differential equations for noise removal, *IEEE Transactions on Image Processing* 9 (10) (2000) 1723-1730.
- [15] A. Araújo, S. Barbeiro, P. Serranho, Stability of finite difference schemes for complex diffusion processes, *SIAM Journal on Numerical Analysis* 50 (3) (2012) 1284-1296.
- [16] A. Araújo, S. Barbeiro, P. Serranho, Stability of finite difference schemes for nonlinear complex reaction-diffusion processes, *IMA Journal of Numerical Analysis* 35 (3) (2015) 1381-1401.
- [17] A. Chambolle, P.-L. Lions, Image recovery via total variation minimization and related problems, *Numerische Mathematik* 76 (2) (1997) 167-188.
- [18] C. Elliott, S. Smitheman, Numerical analysis of the tv regularization and H^{-1} fidelity model for decomposing an image into cartoon plus texture, *IMA Journal of Numerical Analysis* 29 (3) (2009) 651-689.
- [19] L. I. Rudin, S. Osher, E. Fatemi, Nonlinear total variation based noise removal algorithms, *Physica D: Nonlinear Phenomena* 60 (1) (1992) 259-268.
- [20] V. S. Prasath, A. Singh, A hybrid convex variational model for image restoration, *Applied Mathematics and Computation* 215 (10) (2010) 3655-3664.
- [21] Y.-H. R. Tsai, S. Osher, Total variation and level set methods in image science, *Acta Numerica* 14 (2005) 509-573.
- [22] R. Zanella, F. Porta, V. Ruggiero, M. Zanetti, Serial and parallel approaches for image segmentation by numerical minimization of a second-order functional, *Applied Mathematics and Computation* 318 (2018) 153-175.
- [23] H. Amann, Time-delayed perona-malik type problems, *Acta Math. Univ. Comenianae* 76 (1) (2007) 15-38.
- [24] A. Belahmidi, A. Chambolle, Time-delay regularization of anisotropic diffusion and image processing, *ESAIM: Mathematical Modelling and Numerical Analysis* 39 (2) (2005) 231-251.
- [25] Z. Guo, J. Yin, Q. Liu, On a reaction-diffusion system applied to image decomposition and restoration, *Mathematical and Computer Modelling* 53 (5) (2011) 1336-1350.
- [26] H. Luo, L. Zhu, H. Ding, Coupled anisotropic diffusion for image selective smoothing, *Signal Processing* 86 (7) (2006) 1728-1736.

- [27] M. Nitzberg, T. Shiota, Nonlinear image filtering with edge and corner enhancement, *IEEE transactions on pattern analysis and machine intelligence* 14 (8) (1992) 826-833.
- [28] V. S. Prasath, D. Vorotnikov, On a system of adaptive coupled pdes for image restoration, *Journal of mathematical imaging and vision* 48 (1) (2014) 35-52.
- [29] P. Guidotti, Anisotropic diffusions of image processing from perona-malik on, *Advanced Studies in Pure Mathematics* 99 (2015) 20XX.
- [30] S. Osher, A. Solé, L. Vese, Image decomposition and restoration using total variation minimization and the H^{-1} norm, *Multiscale Modeling and Simulation* 1 (3) (2003) 349-370.
- [31] R. Adam, Sobolev spaces, in: *Pure and Applied Mathematics Series of Monographs and Textbooks*, Vol. 65, Academic Press, Inc., New York, San Francisco, London., 1975.
- [32] L. Evans, *Partial Differential Equations*, in: *Graduate Studies in Mathematics*, Vol. 19, American Mathematical Society, Providence, Rhode Island, 1998.
- [33] S. K. Jain, R. K. Ray, A. Bhavsar, *Iterative solvers for image denoising with diffusion models: A comparative study*, Elsevier, 2015.
- [34] J. L. Lions, *Contrôle Optimal de Systèmes Gouvernés par des Équations aux Dérivées Partielles*, Dunod, Paris, 1968.
- [35] M. Chipot, I. Shafrir, V. Valente, G. V. Caffarelli, On a hyperbolic-parabolic system arising in magnetoelasticity, *Journal of Mathematical Analysis and Applications* 352 (1) (2009) 120-131.
- [36] S. Zheng, *Nonlinear parabolic equations and hyperbolic-parabolic coupled systems*, CRC Press, 1995.
- [37] S. K. Jain, R. K. Ray, A. Bhavsar, A comparative study of iterative solvers for image denoising, in: *Proceedings of the 3rd International Conference on Frontiers of Intelligent Computing: Theory and Applications (FICTA) 2014*, Springer, 2015, pp. 307-314.
- [38] J. Sun, J. Yang, L. Sun, A class of hyperbolic-parabolic coupled systems applied to image restoration, *Boundary Value Problems* 2016 (1) (2016) 187.
- [39] A. Buades, B. Coll, J.-M. Morel, A non-local algorithm for image denoising, in: *Computer Vision and Pattern Recognition, 2005. CVPR 2005. IEEE Computer Society Conference on*, Vol. 2, IEEE, 2005, pp. 60-65.
- [40] Z. Wang, A. C. Bovik, H. R. Sheikh, E. P. Simoncelli, Image quality assessment: from error visibility to structural similarity, *Image Processing, IEEE Transactions on* 13 (4) (2004) 600-612.
- [41] X.-C. Tai, K.-A. Lie, T. F. Chan, S. Osher, *Image Processing Based on Partial Differential Equations: Proceedings of the International Conference on PDE-Based Image Processing and Related Inverse Problems*, CMA,Oslo, August 8-12, 2005, Springer Science & Business Media, 2006.